



Inclusion Engineering in Medium Mn Steels: Effect of Hot-Rolling Process on the Deformation Behaviors of Oxide and Sulfide Inclusions

YONG WANG, YONGGANG YANG, ZHIHUA DONG, JOO HYUN PARK, ZHENLI MI, XINPING MAO, and WANGZHONG MU

Medium Mn steel (MMS) is a new category of the third-generation advanced high strength steel (3rd AHSS) which is developed in the recent 1-2 decades due to a unique trade-off of strength and ductility. Thus, this steel grade has a wide application potential in different fields of industry. The current work provides a fundamental study of the effect of hot-rolling on the inclusion deformation in MMS including a varied 7 to 9 mass pct Mn. Specifically, the deformation behavior of different types of inclusions (*i.e.*, Mn(S,Se), liquid oxide (MnSiO₃), MnAl₂O₄, and complex oxy-sulfide) was investigated. The results show that both MnSiO₃ and Mn(S,Se) are soft inclusions which are able to be deformed during the hot-rolling process but MnAl₂O₄ does not. The aspect ratio of soft inclusions increases significantly from as-cast to hot-rolling conditions. When the maximum size of different inclusions is similar, Mn(S,Se) deforms more than MnSiO₃ does. This is due to a joint influence of physical parameters including Young's modulus, coefficient of thermal expansion (α), *etc.* However, when the maximum size of one type of inclusion (*e.g.*, MnSiO₃) is much larger than another one (*e.g.*, Mn(S,Se)), this maximum size of soft inclusions plays a dominant role than other factors. In addition, the deformation behavior of dual-phase inclusion depends on the major phase, *i.e.*, either oxide or sulfide. Last but not least, empirical correlations between the reduction ratio of the thickness of plate, grain size, and aspect ratio of oxide and sulfide inclusions after hot-rolling are provided quantitatively. This work aims to contribute to the 'inclusion engineering' concept in the manufacturing of new generation AHSS.

<https://doi.org/10.1007/s11663-022-02517-2>

© The Author(s) 2022

I. INTRODUCTION

INCLUSION engineering is a comprehensive concept dealing with the control of amount, size distribution, and chemical composition of non-metallic inclusions in the steels^[1] and alloys.^[2] Furthermore, it also concerns the correlation between inclusion, microstructure and property on the quality control of the final product, *e.g.*, advanced high strength steel (AHSS). Recently, AHSS has been widely used in the automotive industry and has attracted wide interest. In particular, medium Mn steel (MMS) which usually contains 3 to 11 mass pct Mn is a new category of third-generation AHSS developed in the recent 1-2 decades due to a unique trade-off of strength and ductility.^[3-6] This steel grade possess a unique combination of strength and ductility derived from a microstructure consisting of ferrite (α) and austenite (γ).^[7,8] There are intense research activities on the microstructure and mechanical properties of medium Mn steels,^[9-12] however, the non-metallic inclusions in these steels have not attracted noticeable attention so far. Grajcar *et al.*^[13] investigated the evolution of inclusion features and their modification using rare

YONG WANG is with the The State Key Laboratory of Refractories and Metallurgy, Wuhan University of Science and Technology, Wuhan, 430081, China and also with the Department of Materials Science and Engineering, KTH Royal Institute of Technology, 100 44, Stockholm, Sweden. YONGGANG YANG is with the Department of Materials Science and Engineering, KTH Royal Institute of Technology and also with the Beijing Advanced Innovation Center for Materials Genome Engineering, National Engineering Research Center for Advanced Rolling Technology, University of Science and Technology Beijing, Beijing, 100083, China. ZHIHUA DONG is with the National Engineering Research Center for Magnesium Alloys, Chongqing University, Chongqing, 400044, China and also with the College of Materials Science and Engineering, Chongqing University, Chongqing, 400044, China. JOO HYUN PARK is with the Department of Materials Science and Engineering, KTH Royal Institute of Technology and also with the Department of Materials Science and Chemical Engineering, Hanyang University, Ansan, 15588, Korea. ZHENLI MI and XINPING MAO is with the Beijing Advanced Innovation Center for Materials Genome Engineering, National Engineering Research Center for Advanced Rolling Technology, University of Science and Technology Beijing. WANGZHONG MU is with the Key Laboratory of Electromagnetic Processing of Materials (Ministry of Education), School of Metallurgy, Northeastern University, Shenyang 110819, China and also with the Department of Materials Science and Engineering, KTH Royal Institute of Technology. Contact e-mail: wmu@kth.se

Manuscript submitted January 5, 2022; accepted April 1, 2022.

Article published online April 26, 2022.

earth elements. They proposed that the Mn content in a range between 3 and 5 mass pct does not affect the inclusion type. Yu *et al.*^[14] studied the evolution mechanism of inclusions in MMS by Mg treatment with different aluminium contents, and they found that the large cluster-like Al₂O₃ inclusions transformed into finely dispersed Mg-containing inclusions. Park *et al.*^[15] reported the formation mechanism of inclusions in Fe-xMn-yAl alloys (x = 10 and 20 pct, y = 1, 3, and 6 pct). Besides, the effect of Al content on the reaction between high-Mn steel and CaO-SiO₂-Al₂O₃-MgO slag or flux has been quantitatively investigated.^[16–18] However, there are only a few works that focus on the effect of Mn content on the non-metallic inclusion composition and size evolution in MMS. Moreover, there is no attempt has been made to investigate other inclusion features, *e.g.*, deformability.

Deformation plays an important role in leading to the effect of transformation-induced plasticity (TRIP) in MMS, strain-induced martensite has been investigated comprehensively in this steel grade.^[19,20] Besides, many factors can influence the deformability of inclusions, including composition, size, melting point temperature,^[21,22] viscosity,^[23,24] plasticity (*i.e.*, the ratio between the deformation of inclusions and the deformation of steel matrix),^[22,25] and micro-hardness.^[26] Luo and Ståhlberg^[27] analyzed the deformation behavior of MnS inclusions in the plate rolling process under different temperatures, friction and rolling schedules by finite element method (FEM). However, many assumptions were included in their numerical simulations. Wang *et al.*^[28,29] qualitatively described the deformation of dual-phase (MnO-SiO₂-Al₂O₃ + SiO₂) inclusions in tire cord steels based on experimental investigations. They found that MnO-SiO₂-Al₂O₃ inclusions were deformed severely during the hot rolling, while SiO₂ was very hard to be deformed. Moreover, Zhang *et al.*^[21] and Yang *et al.*^[22] systematically studied the deformation of inclusions in tire cord steels during hot rolling. They reported that the aspect ratio obtained after the first hot-rolling process was used to characterize the high-temperature deformability of MgO-Al₂O₃-SiO₂-CaO inclusions owing to the fracture of the inclusions with the increasing reduction ratio of the steel during hot rolling. Wang *et al.*^[30,31] investigated the deformation behavior of inclusions in the solid steel at different temperatures and in the semi-solid steel, they reported that the hardness difference between inclusions and the steel matrix directly influenced the deformation of inclusions. Nevertheless, few attempts were made to quantitatively compare the deformation behaviors of different types of inclusions (oxide, sulfide, *etc.*) during the hot rolling process. Furthermore, the mechanism of different deformation behaviors of oxide and sulfide inclusions was not investigated clearly.

In the present work, lab-scale MMSs were manufactured to investigate the deformation behavior of different types of inclusions. To obtain a general understanding of this grade steel, a series MMSs with various Mn contents ranging from 7 to 9 mass pct were selected. The influence of the hot rolling process on the deformability features (*i.e.*, aspect ratio, deformation

index, *etc.*) of different inclusions was discussed. Further, effects of physical parameters (*i.e.*, micro-hardness, Young's modulus, coefficient of thermal expansion (CTE), *etc.*) as well as the maximum size on the inclusion deformability were quantitatively discussed. This systematic study aims to reveal the mechanism of different behaviors of various inclusions during hot rolling. In addition, the empirical relationships between the thickness of the plate, prior austenite grain size (PAGS), and the aspect ratio of different types of inclusions were proposed. The obtained understanding aims to correlate the physical properties, inclusion particles and microstructure quantitatively, as well as to contribute to 'Inclusion Engineering' in the third-generation AHSS.

II. METHODOLOGY

A. Alloy Preparation

Lab-scale MMS samples (~5 kg) were prepared in a medium frequency vacuum induction furnace with a rated power of 100 KW. The maximum vacuum degree is 6.7×10^{-3} Pa. As-cast steel billet with a thickness of 35 mm was hot-rolled to a final thickness of 3.5 mm with four rolling passes, as schematically shown in Figure 1. Starting and finishing rolling temperatures were 1100 °C and 800 °C, respectively. The chemical compositions of the investigated MMS samples with as-cast and after hot rolling conditions are listed in Table I.

B. Characterization

The inclusions in the as-cast and hot-rolled samples were examined by the electrolytic extraction (EE) method using a 10 pct AA (10 pct acetylacetone-1 pct tetramethylammonium-methanol) electrolyte.^[32] After extraction, the solution containing inclusions was filtrated through a polycarbonate (PC) membrane film filter with an open pore size of 0.4 μm. Thereafter, the characteristics (morphology, size, number, and composition) of the inclusions were investigated using a scanning electron microscopy in combination with energy dispersive spectroscopy (SEM-EDS). 60 images obtained under a 1000x magnification were taken by the method of continuous field of view in each sample to analyze the inclusion frequency and number density. The average diameter (d_v) of inclusions was calculated to be half of the sum of maximum length (L) and maximum width (W) of inclusion measured on SEM images.

The microstructure of both as-cast and hot-rolled samples were characterized by electron backscatter diffraction (EBSD). The samples for EBSD analysis were mechanically ground using fine SiC papers (320#, 600# and 1200#), followed by an electrolytic polishing process. The used polishing electrolytic was a perchloric acid solution (20 pct HClO₄ + 80 pct C₂H₅OH). The e-FLASH HR (Bruker) EBSD detector in a field emission scanning electron microscope (FE-SEM) (JEOL JSM-7800F) was used. The microscope was

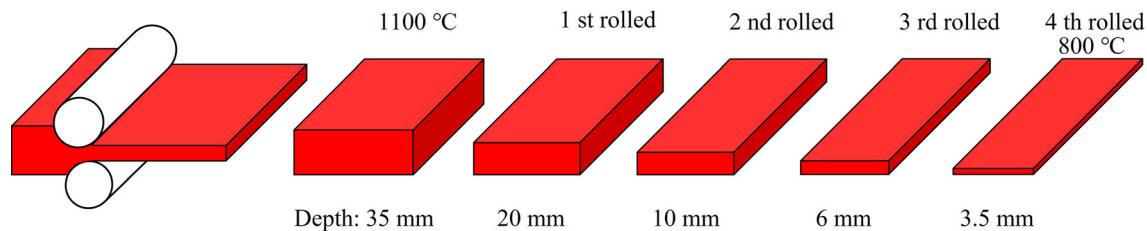


Fig. 1—Schematic illustration of the hot rolling process.

Table I. Chemical Compositions of the Proposed Steels With Different Conditions (Mass Pct)

	C	Mn	Si	O	N	S
7Mn-C	0.205	6.7	1.5	0.0033	0.005	0.011
7Mn-R	0.174	6.7	1.5	0.0045	0.007	0.010
8Mn-C	0.210	8.3	1.5	0.0031	0.008	0.005
8Mn-R	0.178	8.3	1.5	0.0050	0.010	0.006
9Mn-C	0.213	9.1	1.6	0.0043	0.005	0.006
9Mn-R	0.180	9.2	1.6	0.0037	0.006	0.006

*C represents as-cast, R represents as-rolled, Al is <0.003 mass pct, Se is <0.001 mass pct.

operated at an acceleration voltage of 15 kV and using a $0.5 \mu\text{m}$ step size for the as-cast sample and $0.05 \mu\text{m}$ step size for the hot-rolled sample. Quantax (Bruker) software was used for the initial EBSD data processing. Post-processing and analysis of EBSD data were performed using the MATLAB-based Toolbox MTEX 5.4.0.^[33,34] A quenching dilatometer (Linseis, DIL L78RITA) was used for detecting the phase transformation temperatures during heating and cooling. The steel specimens were machined to a geometry of $3 \times 3 \times 10 \text{ mm}$. The samples were heated to $1100 \text{ }^\circ\text{C}$ with a rate of $5 \text{ }^\circ\text{C}/\text{seconds}$, and were subsequently cooled with different cooling rates of 5, 10 and $50 \text{ }^\circ\text{C}/\text{seconds}$ using He. Temperatures of A_1 (Austenite transformation starting temperature), A_3 (Austenite transformation finishing temperature) and M_s (martensite starting temperature) were detected. Besides, a high-resolution dilatometer (Netzsch DIL 402 SUPREME Expedis) was used to measure the coefficient of thermal expansion (CTE) of the proposed MMSs, the samples were machined to be a bar with $4 \times 4 \times 12 \text{ mm}$. The heating and cooling rates were set as $5 \text{ }^\circ\text{C}/\text{min}$. Ar (purity >99.999 mass pct) with a flow rate of $50 \text{ ml}/\text{min}$ was filled in the chamber to avoid oxidation. Details can be seen in Reference 35. The reason for switching to a high-resolution dilatometer is due to the CTE measurement needs to be done using a very slow heat and cooling condition, which closes to the equilibrium state.

C. Theoretical Calculations

Thermodynamic calculation software, Thermo-Calc 2020b^[36] with a TCFE10 database^[37] was used to predict the inclusion formation in MMSs. Calculations of bulk modulus (B), Shear modulus (G), and Young's

modulus (E) were performed in the framework of density functional theory (DFT)^[38] as implemented in the exact muffin-tin orbital (EMTO) method.^[39,40] Details of the calculations can be seen in Reference 41.

III. RESULTS

A. Inclusion Composition

In this study, the observed inclusions are classified into three groups according to their chemical compositions, *i.e.*, type 1: Mn(S,Se); type 2: oxide inclusions which consisted of dominant liquid oxide, termed as MnSiO_3 from herein, with a core of MnAl_2O_4 ; type 3: mixed inclusions containing different oxides and Mn(S,Se).

The representative morphologies and the EDS spectra of typical inclusions in the as-cast and hot-rolled samples are shown in Figure 2. In the as-cast samples, Mn(S,Se) inclusion is one of the major types of inclusions. According to the EDS analysis, the average Se content in these inclusions is 7.1 mass pct. Se is from the impurity of raw materials to produce these steel samples, since Se is usually contaminated in electrolytic manganese, and SeO_2 is commonly used as an additive in aqueous electrolysis.^[42] In addition, the MnS and MnSe were reported to have the same FCC structures.^[43] In this case, the property of Mn(S,Se) is very close to MnS type inclusion. Besides, this type Mn(S,Se) inclusion also has been found in high-Mn steels^[15] as well as CoCrFeMnNi high-entropy alloys^[41] manufactured using electrolytic manganese.^[44] Type 2 inclusions consist of two different types of oxide inclusions, *i.e.*, a single liquid oxide (MnSiO_3) inclusion and a mixed one consisting of MnAl_2O_4 and MnSiO_3 inclusions. The average compositions of these two oxides are 24 mass pct MnO-76 mass pct Al_2O_3 and 39 mass pct MnO-61 mass pct SiO_2 , respectively. The Al content is from the impurity of raw materials. Specifically, the chemical elemental mappings of a typical type 2 inclusion are shown in Figure 3(a). It is seen that the MnAl_2O_4 core is covered by MnSiO_3 inclusions. It is able to postulate that the MnAl_2O_4 forms in the liquid steel subsequently the liquid oxide (MnSiO_3) covers it during the collision. Type 3 inclusion is the mixed-type with oxide core (type 2) and Mn(S,Se) (type 3), the elemental mapping of this type of inclusions are shown in Figure 3(b). They were formed due to the fact that Mn(S,Se) inclusions precipitated on the surface of oxides during the solidification and in the solid-state.

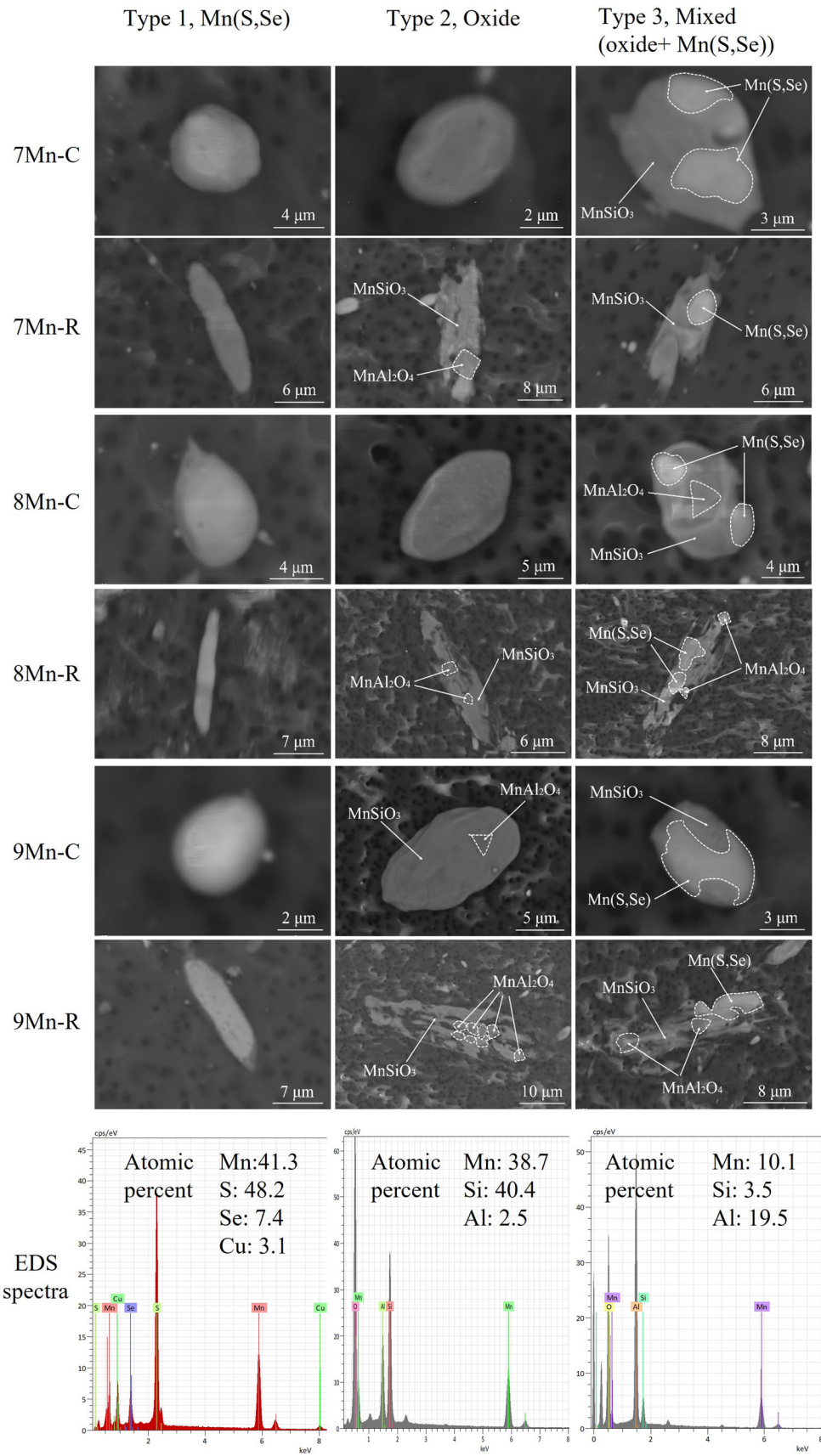


Fig. 2—Morphology of typical types of inclusions in different MMSs.

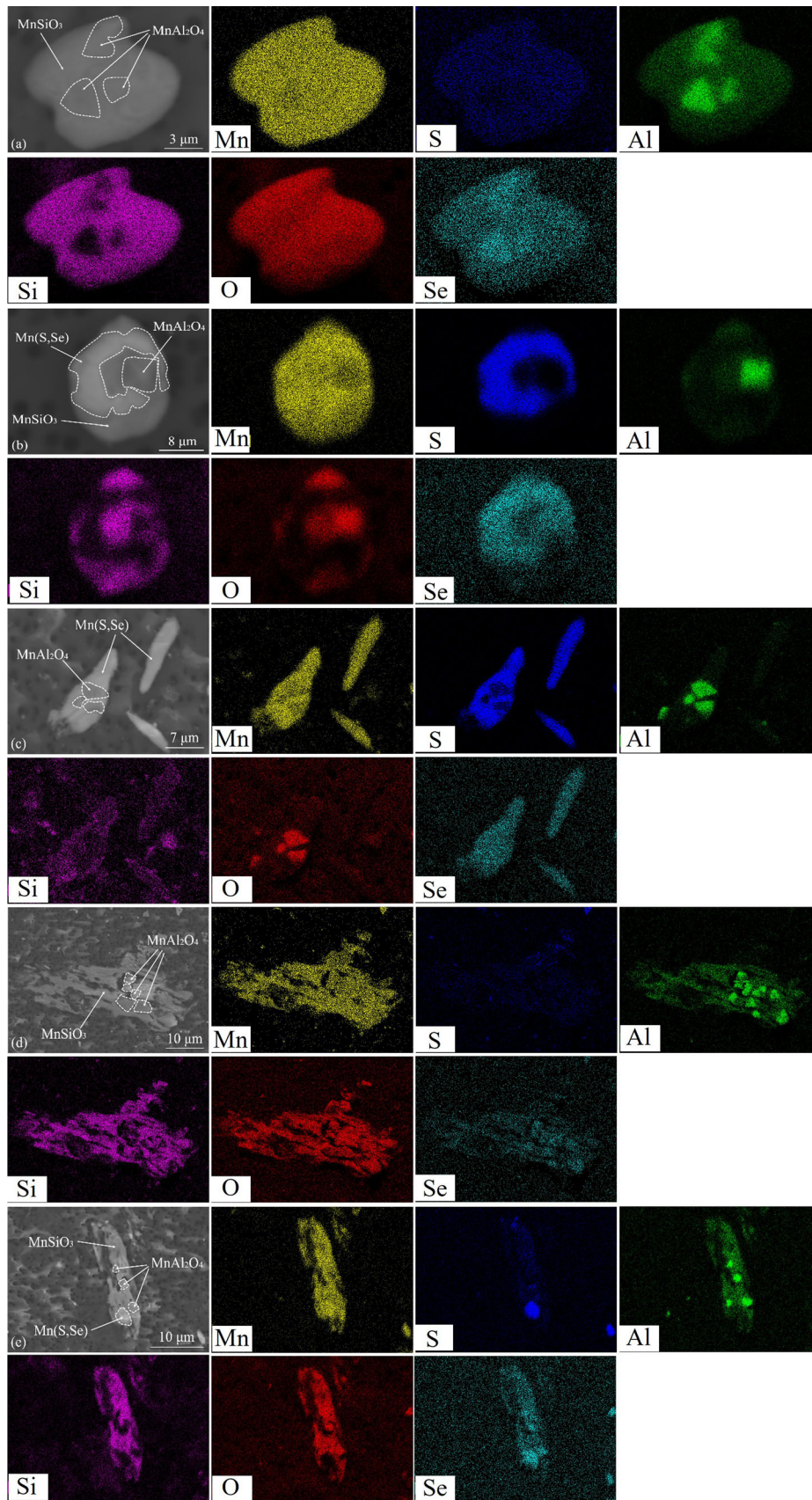


Fig. 3—Elemental mappings of typical inclusions in as-cast samples (a) oxide, (b) the mixed-type and in hot-rolled samples (c) Mn(S,Se), (d) oxide, (e) the mixed-type.

In hot-rolled samples, Mn(S,Se) inclusions have certainly been elongated to become strings on the cross-section in the rolling direction, the elemental mappings of this type inclusion are shown in Figure 3(c). For the cases of oxide and mixed inclusions, the related elemental mapping images are shown in Figure 3(d) and (e). Sometimes type 2 and 3 inclusions were easily broken into several separated inclusions due to the different deformability of MnAl_2O_4 and MnSiO_3 inclusions. The deformation behavior of different types of inclusions is discussed in details in Section B of Discussion chapter.

B. Inclusion Number and Size Evolution

The frequency of each group of inclusions in the as-cast and hot-rolled samples was determined by the number of inclusions on the filters, as shown in Figure 4. The majority of inclusions in the as-cast steel samples is Mn(S,Se), which accounts for almost 50 pct of total inclusions, as shown in Figure 4(a). In addition, the total frequency of oxide and mixed types of inclusions slightly increases from 42 pct in 7Mn sample to 54 pct in 9Mn sample, which is closely correlated with the oxygen contents in these samples. The number frequency of Mn(S,Se) inclusions increase in all the samples after hot rolling, as shown in Figure 4(b). Especially, the number densities of Mn(S,Se) inclusions are 7910 and 25300 mm^{-3} in as-cast and hot-rolled 7 Mn samples, respectively. One reason is Mn(S,Se) can form in the range of starting rolling temperature (1100 °C). In addition, the segregation and enrichment of sulfur during the hot rolling process may occur to form more sulfides. It should be mentioned that the increase of Mn(S,Se) inclusions in 7Mn sample is higher than those in the other two samples. This can be explained by the fact that the actual sulfur content in 7Mn sample is higher than that in the other two samples, which can result in more Mn(S,Se) inclusions formation.

Furthermore, the size and number of inclusions were systematically investigated in the as-cast and hot-rolled samples. Figure 5 presents the number fractions and the average sizes of the three groups of inclusions in

different as-cast samples. It is found that the size range of the majority (>90 pct) of inclusions in all samples is 1 to 9 μm . The size ranges of oxide and mixed inclusions (1 to 15 μm) are slightly wider than that of Mn(S,Se) inclusions (1 to 12 μm). This is due to the fact that some large size oxide and mixed inclusions having $d_v > 9 \mu\text{m}$ were found in 8Mn and 9Mn samples but not in 7Mn sample. The reason can be due to more MnSiO_3 inclusions formed in the 8Mn and 9Mn alloys according to a higher Mn content, and the formed inclusions are easier to agglomerate and form the large size cluster. The agglomeration potency of this type of inclusion has been reported elsewhere.^[45,46] In addition, the average sizes of oxide and mixed inclusions are quite close, which are about 4.7 μm and 4.3 μm in 8Mn and 9Mn samples and 3.6 μm in 7Mn sample. In terms of Mn(S,Se) inclusions, their average size is slightly larger in 7Mn sample (4.8 μm) than the value in 8 Mn (4.2 μm) and 9Mn (4.3 μm) samples, as shown in Figure 5(d).

The number fractions of the three groups of inclusions in different hot-rolled samples are presented in Figure 6. It should be noted that a small number of oxide and mixed inclusions having the sizes larger than 20 μm were also found in 8Mn and 9Mn samples while not in 7Mn sample. To better compare the distribution of inclusions in the three samples, the size of inclusions less than 20 μm was considered. The number of super large ones is quite low. The majority of the Mn(S,Se) inclusions have the sizes smaller than 10 μm , which is similar to those in as-cast samples. It is indicated that the size ranges of Mn(S,Se) inclusions were not significantly changed during the hot-rolling process. A relatively larger fraction of small-sized Mn(S,Se) inclusions were found in 8 Mn sample than the other two samples. Last but not least, it is found that the fraction of the oxide and mixed types of inclusions with the larger sizes ($d_v > 10 \mu\text{m}$) in 8 Mn and 9 Mn samples are larger than that in 7 Mn sample, which is a consistent finding as the one in the as-cast samples. In addition, there might be more Mn-contained inclusions from the surface of the existed one during the hot-rolling, especially Mn(S,Se), which enlarge the size of the existed inclusions.

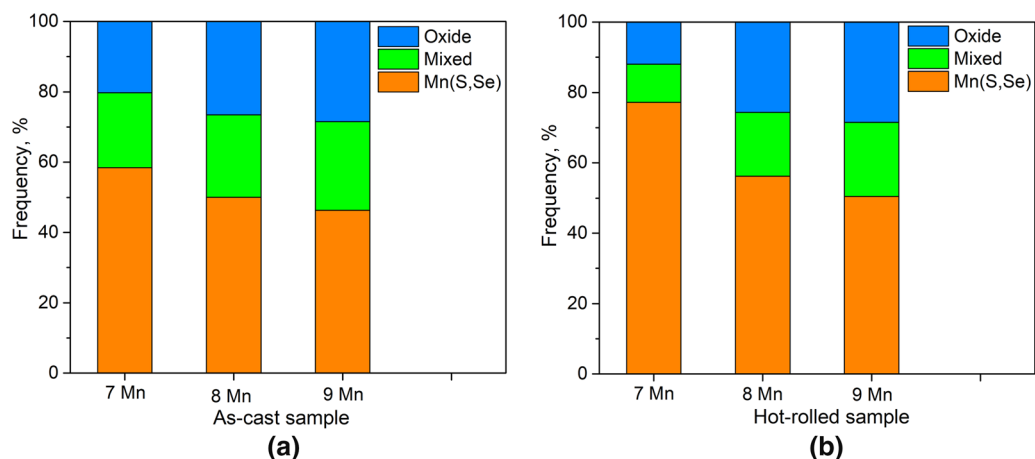


Fig. 4—Frequency of different types of inclusions in (a) as-cast and (b) hot-rolled samples.

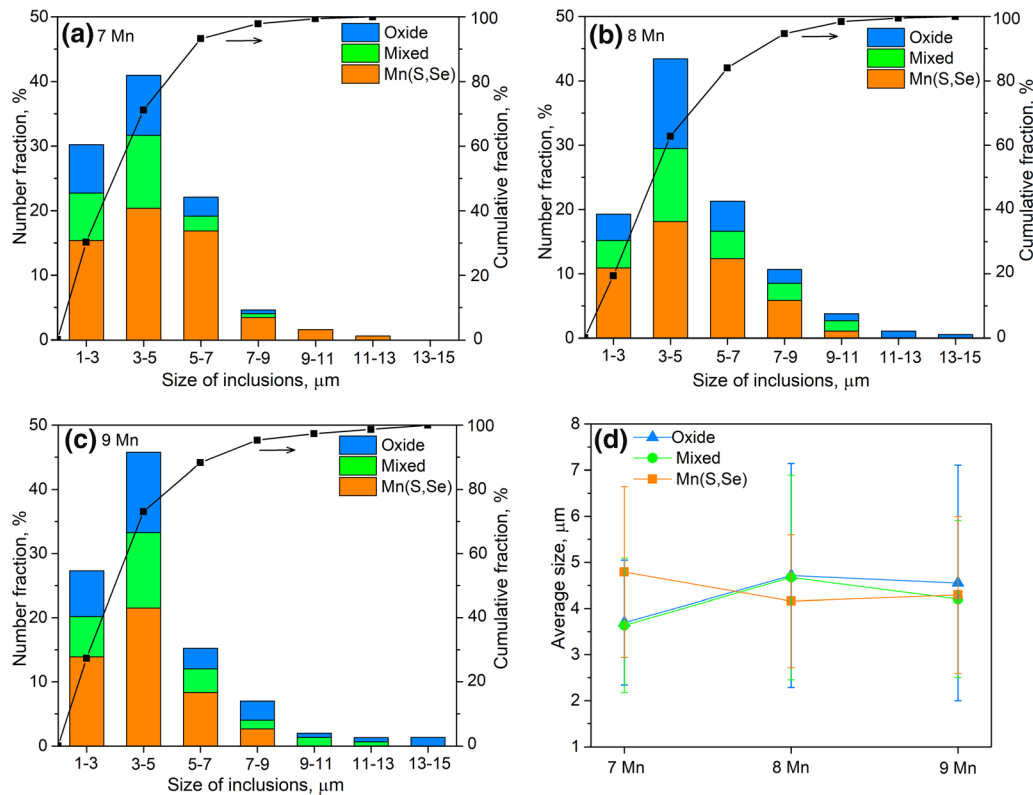


Fig. 5—Number fraction of the three groups of inclusions in as-cast (a) 7 Mn, (b) 8 Mn and (c) 9 Mn samples and average size (d) of different inclusions in the three as-cast samples.

C. Inclusion Morphology Evolution After Hot Rolling

During the hot-rolling process, the morphology evolution of inclusion is presented by aspect ratio (AR = length/width). In the as-cast samples, three types of inclusions show similar morphology, as shown in Figure 2. Specifically, the average ARs for Mn(S,Se), mixed and oxide inclusions are 1.28, 1.47 and 1.54, respectively. While after hot rolling, the deformability of these three types of inclusions is quite different, as shown in Figure 3. Most of the Mn(S,Se) inclusions show a strip shape, where the mixed and oxide types present a thin plate-like shape. To better understand the deformation behavior of different types of inclusions, the deformation index of inclusions after hot rolling is introduced, according to Malkiewicz and Rudnik.^[47] It is expressed by Eq. [1]:

$$v = \frac{\varepsilon_i}{\varepsilon_s} = \frac{\frac{2}{3} \ln \frac{\lambda_1}{\lambda_0}}{\ln \frac{h_0}{h_1}} \quad [1]$$

where v is the deformation index, ε_i and ε_s are the true strain of the inclusion and steel matrix, respectively; λ_1 and λ_0 are the average aspect ratios of inclusions before and after hot rolling; h_0 and h_1 are the thickness of the steel before (35 mm) and after hot rolling (3.5 mm).

Figure 7 shows (a) the average and maximum sizes of inclusions and the aspect ratio (AR) and (b) the deformation index (DI) of different types of inclusions in hot-rolled samples. It is seen that the average and maximum sizes of oxide and mixed inclusions in 7 Mn

samples are smaller than those in 8 Mn and 9 Mn samples. This can be explained by the fact that larger size oxide and mixed inclusions were observed in 8 Mn and 9 Mn samples. It is worth noting that larger values of the ARs and DIs of oxide and mixed inclusions are found in 8 Mn and 9 Mn samples than those in 7 Mn sample. Moreover, even though the average sizes of mixed inclusions are smaller compared to oxide inclusions, the ARs and DIs of mixed inclusions are larger than those of oxide inclusions. This can be attributed to the contribution of the deformation of Mn(S,Se) inclusions. In terms of Mn(S,Se) inclusions, their average and maximum sizes decrease in the following order: 7 Mn, 9 Mn and 8 Mn. Specifically, the average size of them in 7 Mn and 9 Mn samples are 4.8 and 4.3 μm , while that in 8 Mn sample is 3.5 μm . In addition, the average AR of Mn(S,Se) inclusions in 7 Mn sample is about 3.6, which is larger than those in 8 Mn (2.5) and 9 Mn (2.7) sample. This means the deformation of Mn(S,Se) inclusions is larger in 7 Mn sample. Moreover, the size of Mn(S,Se) inclusions can be related to the sulfur content in the samples. A previous study^[48] showed that higher sulfur content resulted in higher aspect ratios of elongated MnS inclusions after hot rolling. The AR changes of Mn(S,Se) and oxide inclusions show some differences in different samples after rolling. Specifically, the average ARs of Mn(S,Se) inclusions are smaller than those of oxide inclusions in 8 Mn and 9 Mn samples, while the opposite tendency is found in 7 Mn sample. This interesting issue is due to the difference in the maximum size of oxide and mixed inclusions.

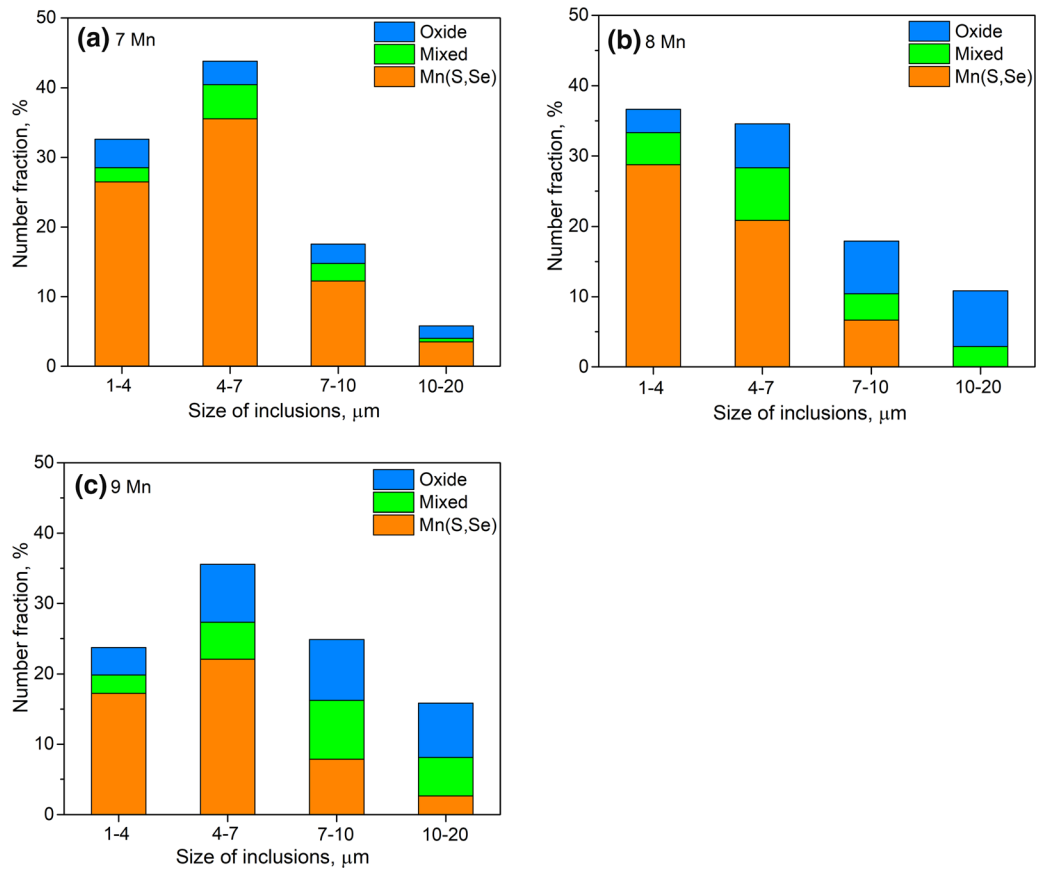


Fig. 6—Number fraction of the three groups of inclusions in hot-rolled (a) 7 Mn, (b) 8 Mn and (c) 9 Mn samples.

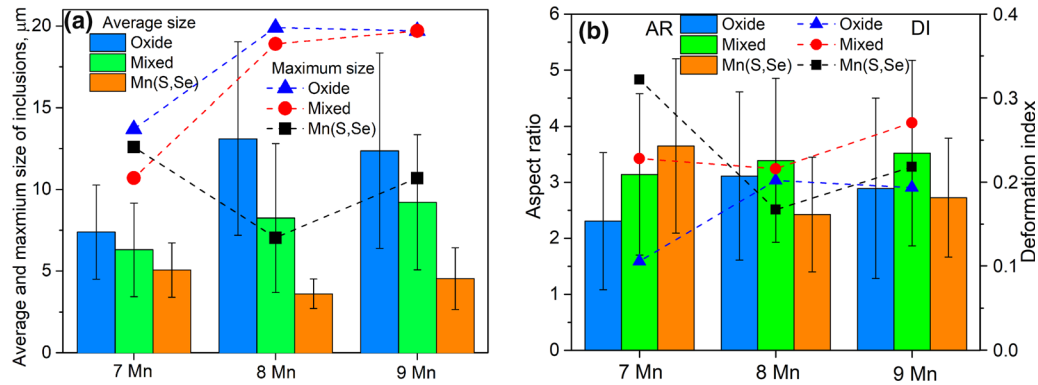


Fig. 7—Average and maximum size of inclusions (a) and aspect ratio and deformation index of inclusions (b) in hot-rolled samples.

IV. DISCUSSIONS

A. Effect of Mn Content on the Inclusion Composition and Size Evolution

In the former section, it is found that the inclusion size and morphology present different features in the MMSs containing different Mn contents, however, the inclusion composition does not change much when the Mn content increases from 7 to 9 Mass pct. This section investigates this fact by thermodynamic consideration.

Equilibrium calculation of different phase formations in the as-cast 7 Mn and 9 Mn steels are expressed in Figures 8(a) and (b), based on the chemical compositions in Table I. The solidus and liquidus temperatures of 7 Mn and 9 Mn steels are also presented, respectively. It is seen that the temperature of 7 Mn steel are slightly higher than that of 9 Mn steel. The thermodynamic calculations predict the liquid oxide is the stable inclusion in the liquid state of both steels. In addition, the atomic ratio of Mn/Si in the liquid oxide does not

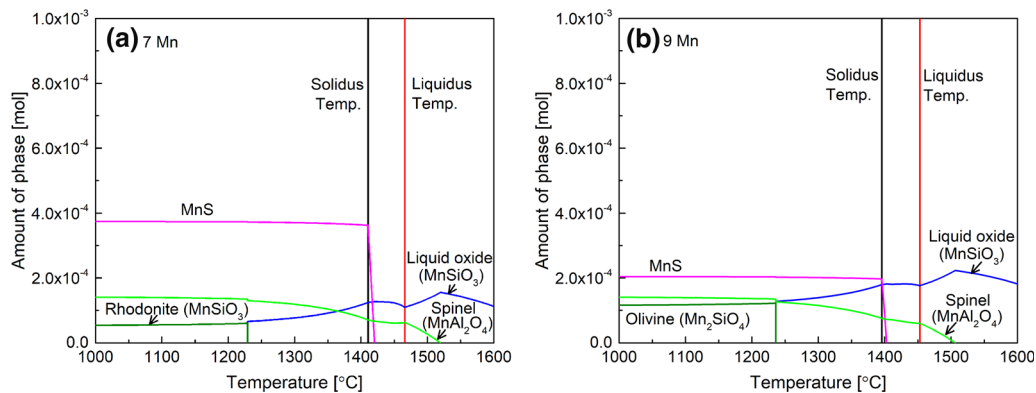


Fig. 8—Equilibrium calculations of different phases formation in (a) 7 Mn and (b) 9 Mn steels.

always express a fixed value of 1.0, but ranges from 1 to 1.5. However, these ratios are slightly higher in 9 Mn steels due to a higher Mn in the matrix. According to SEM-EDS results, Mn/Si atomic ratio of the observed inclusions is slightly over 1.0 in 7 Mn steel, and this value ranges between 1.0 and 1.6 in inclusions in 9 Mn steel, which exactly fits the calculation results. To clarify, even if Mn/Si ratio varies slightly, the liquid oxide inclusion is still one phase but not a different phase, from herein, we use MnSiO₃ to represent the liquid oxide.

Besides the chemical composition, the amount of liquid oxide is higher in 9 Mn steel, which is believed due to the different levels of both Mn and O contents in different steels. In addition, the equilibrium calculation results show that the liquid oxide transfers to Rhodonite (MnSiO₃) in 7 Mn steel and Olivine (Mn₂SiO₄) in 9 Mn steel in solid-state. Thermodynamically, this is due to different levels of Mn content in the matrix. However, this type of oxide is not found in the actual experimental results, since the transformation at a low-temperature range of the equilibrium state needs extremely sufficient time to occur, and this is far from the as-cast condition. In addition, Mn(S,Se) precipitate is predicted to start at 1420 °C (7 Mn steel) and 1405 °C (9 Mn steel), which indicates Mn(S,Se) is mainly formed during the solidification. So the increase of number density of Mn(S,Se) inclusions during the hot-rolling process can be explained from this aspect. The amount of MnS in 7 Mn steel is higher, which is mainly due to the different levels of S in the matrix. This finding also fits the MnS fraction in different steels in experimental results presented in Figures 4 and 6. In addition, MnAl₂O₄ and Mn(S,Se) inclusions were found in the experimental results. However, they are formed due to the impurity elements Al and Se in the raw materials. Since their concentrations are quite low, *i.e.*, Al is less than 0.003 mass pct and Se is less than 0.001 mass pct. For the current calculation, the amount of Al in the matrix is estimated as 0.002 mass pct and the formation of MnAl₂O₄ is able to be predicted in the liquid steels. So solid MnAl₂O₄ inclusions can act as the cores for the MnSiO₃ inclusions, which forms a mixed oxide inclusion. Se is not included in TCFE10 database, only MnS but not Mn(S,Se) is predicted in Figure 8.

B. Effect of Inclusion Size on Its Deformation Behavior After Hot Rolling

Based on above discussions, the chemical composition of oxide inclusions in different MMs is almost the same. However, the fractions of the inclusions in different steels are different, due to a joint effect of both Mn content and impurity levels. The larger amount of liquid oxide inclusion has a larger chance to collide together and form the super large size inclusions. Subsequently, the presence of super large size liquid oxide (MnSiO₃) and mixed inclusions in 8 Mn and 9 Mn steels is easier to deform during hot rolling. This is due to the increased inclusion size leads to a significant stress concentration surrounding the inclusions during rolling.^[49] In addition, both the average size, maximum size and number fraction of Mn(S,Se) in 8Mn and 9Mn steels are much lower than those of liquid oxide inclusion, which is also the reason why the aspect ratio (AR) and deformation index (DI) of super large size MnSiO₃ are much higher than those of Mn(S,Se). It should be pointed out that the current finding only fits for the ‘soft’ inclusions, *e.g.*, oxides including a high concentration of SiO₂, sulfides, *etc.* which are able to be deformed during rolling, but not ‘hard’ inclusion (*e.g.*, MnAl₂O₄, Al₂O₃, *etc.*) which will not deform but crack. This fact has been predicted by a numerical simulation in Reference 50.

C. Effect of Physical Properties on the Inclusion Deformation After Hot Rolling

The previous section discussed that the super large inclusion size could play a dominant role in the inclusion deformation, compared with other influencing factors. However, when the size of different types of soft inclusions is similar, the experimental finding is different. For example, Mn(S,Se) inclusions show a larger DI and AR compared to those of oxide and mixed inclusions in 7 Mn sample, as expressed in Figure 7. The main driving force of inclusion deformation is the stress transferred from the steel matrix. The intrinsic reason for the different deformation behavior of different inclusions is supposed to be the brittle (elastic) to ductile (plastic) transition phenomenon. When the inclusion deforms during the hot-rolling process, elastic

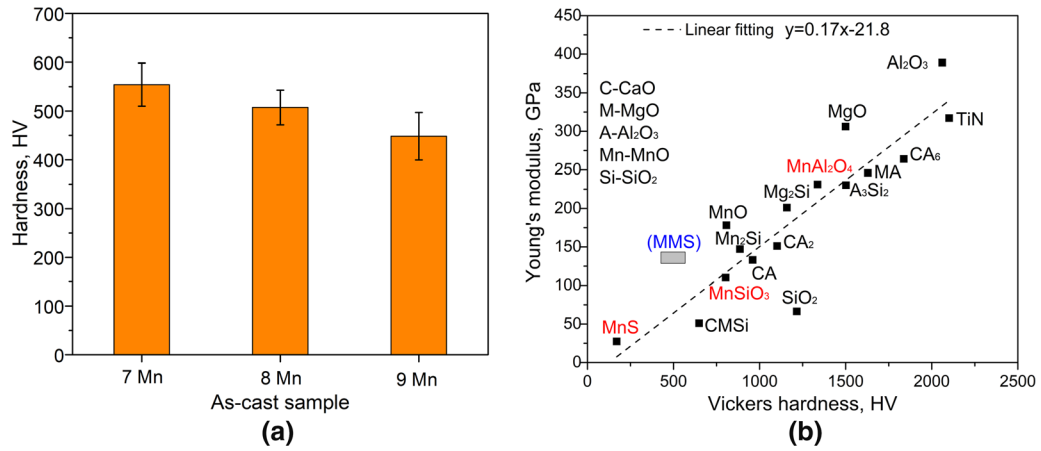


Fig. 9—(a) The measured hardness of different as-cast samples and (b) the correlation between Vickers hardness and Young's modulus of different inclusions, where M represents Mg, C represents Ca, A represents Al, Mn represents MnO, and Si represents SiO₂.

Table II. Bulk Modulus (B), Shear Modulus (G), and Young's Modulus (E) in Medium Mn Steels, Calculated by DFT

Samp.	Bulk Modulus, B (GPa)			Shear Modulus, G (GPa)			Young's Modulus, E (GPa)		
	900 °C	1000 °C	1100 °C	900 °C	1000 °C	1100 °C	900 °C	1000 °C	1100 °C
7Mn	84.5	81.0	78.7	59.9	56.1	53.8	145.4	136.7	131.4
8Mn	80.3	76.6	74.2	59.2	55.3	52.9	142.5	133.7	128.3
9Mn	78.7	74.8	72.4	58.8	54.9	52.6	141.3	132.4	127.0

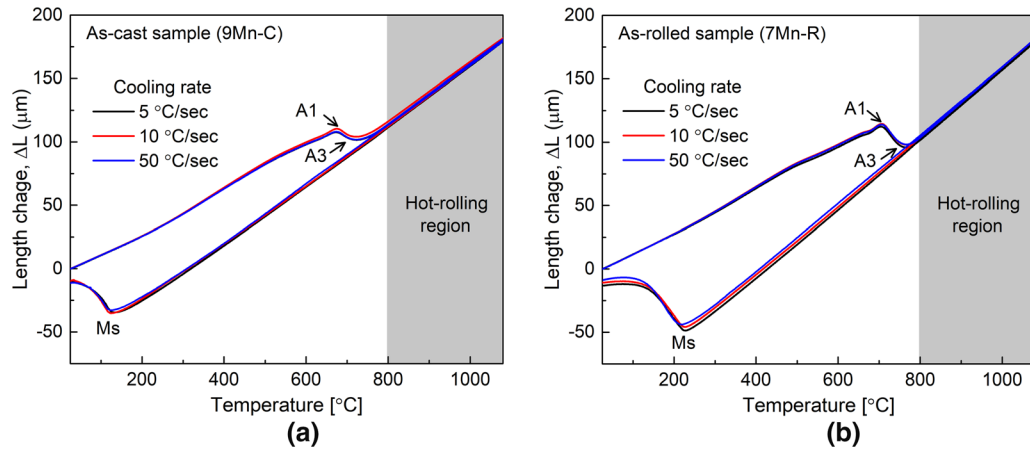


Fig. 10—Dilation curves with different cooling rates in typical (a) as-cast and (b) hot-rolled samples.

Table III. Summary of Phase Transformation Temperatures in Medium Mn Steels

Sample Grade	A ₁ (°C)	A ₃ (°C)	M _s (°C)		
	HR: 5 °C/s	HR: 5 °C/s	CR: 5 °C/s	CR: 10 °C/s	CR: 50 °C/s
7Mn-C	693	754	219	217	211
8Mn-C	684	749	156	151	145
9Mn-C	676	729	137	134	132
7Mn-R	708	760	233	231	228
8Mn-R	680	742	150	148	139
9Mn-R	675	722	110	109	106

deformation occurs firstly followed by plastic deformation if the applied stress exceeds the elastic limit. It is revealed that the physical properties between inclusions and the steel matrix, *e.g.*, micro-hardness, Young's modulus, and thermal expansion coefficient (CTE), *etc.* contribute a more significant role on the inclusion deformation during hot rolling. Details of the influence of physical parameters will be quantitatively discussed in this section. It needs to be mentioned that the physical parameters of Mn(S,Se) are not available in the open literature so the parameters of MnS are used instead.

1. Effect of micro-hardness and Young's Modulus

It is reported that the deformation index of oxide inclusions during hot rolling was inversely proportional to their melting points.^[21] It should be noted that the deformability of different types of inclusions during hot rolling is not limited to the melting points of inclusions. For instance, the melting temperature of MnS is higher than that of MnSiO₃, but they are well deformed during the hot-rolling process. Moreover, most inclusions should be solid during the hot-rolling process, so the effect of the melting point on inclusion deformability is not the main reason. Therefore, this can be explained from the view of hardness or Young's modulus at different temperatures. The hardness of a crystal is the ability to resist plastic deformation due to the hydrostatic compression, and tensile loading.^[51] Young's modulus refers to the ratio of stress to strain in the elastic deformation range of material.

Since the hot-rolling starts with the as-cast sample, the micro-hardness of the as-cast steel matrix is presented in Figure 9(a). It is seen that the measured hardness of the three steels is at the same level of 450 to 550 HV, specifically it slightly decreases due to the increase of Mn content. This range represents the micro-hardness of the matrix. Furthermore, the calculated bulk modulus (B), Shear modulus (G), and Young's modulus (E) of these MMSs samples at different temperatures related to the hot-rolling process are presented in Table II. It can be seen that their values slightly decrease with the increase of Mn content regardless of temperatures, which is in agreement with the measured micro-hardness. The values of the

hardness and Young's modulus for different inclusions are presented in Figure 9(b). The data of inclusions are from References 52 through 57. It is seen that Young's modulus is proportional to the hardness of the inclusion, which was also reported by Jiang *et al.*^[58] The Young's modulus of MnS and MnSiO₃ inclusions are smaller than that of steel.

It is seen that the hardness of MnS is much lower than the value of the steel matrix, which indicates it is quite soft and easy to deform. Alternatively, that value of MnSiO₃ is larger than that of the steel matrix, but the difference is not large. It is able to judge MnSiO₃ can deform during hot rolling. However, the hardness difference might result in their different morphologies after the hot rolling, where the most oxide and mixed typed inclusions showed the plate-like shape with some unconnected parts. To quantitatively evaluate the deformation capability of different inclusions, Young's modulus is used. It is seen that the Young's modulus of MnSiO₃ is about 100 GPa, and that of MnS is around 25 GPa. The smaller Young's modulus leads to the fact

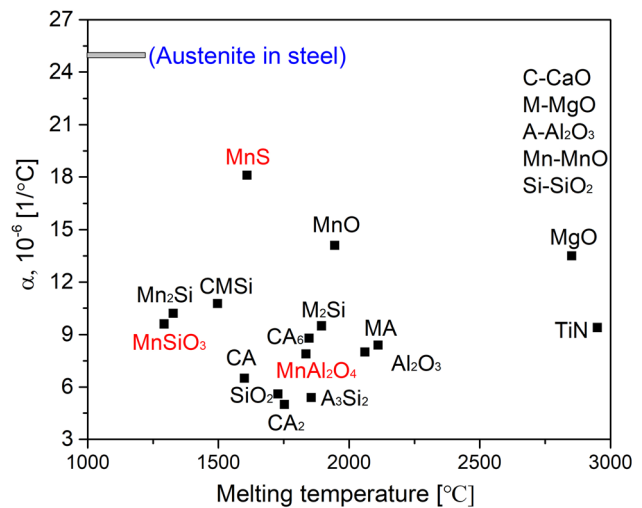


Fig. 12—Coefficient of thermal expansion of different inclusions, data of austenite is based on the dilatometric analysis, data of inclusions is from Refs. [52] and [54].

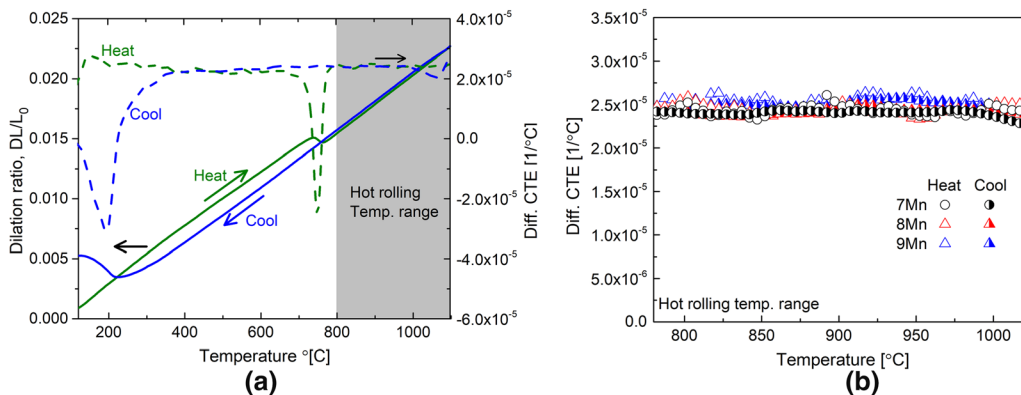


Fig. 11—Measured coefficients of thermal expansion of different samples, (a) typical dilation curve and differential CTE during heating and cooling in 9Mn steel, and (b) the summarized differential CTE in all the three steel grades.

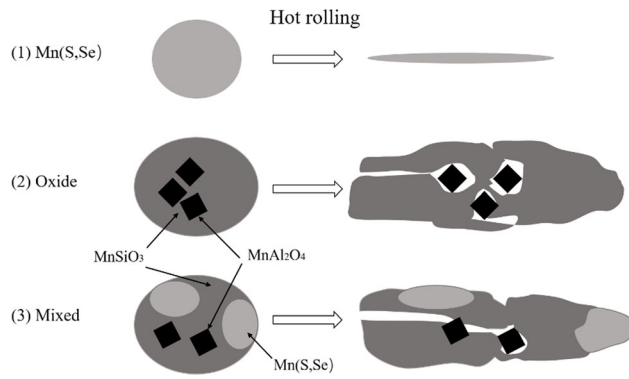


Fig. 13—Schematic illustration of the deformation behavior of different inclusion during the hot rolling process.

that inclusion is easier to deform. In addition, the MnAl_2O_4 spinel inclusions surrounded by the liquid oxide exhibited an octahedral shape, which is one of the typical morphologies of spinel structures. They keep their original morphology without significant changes after hot rolling due to their large hardness and large Young's modulus values compared to those of the steel matrix.

2. Effect of thermal expansion coefficient between inclusions and matrix

Another important physical property influencing the inclusion deformation behavior is the thermal expansion coefficient. Anmark *et al.*^[57] proposed that the magnitude of the effect of inclusions on the improvement of the machinability of the steel matrix depends on the difference of thermal expansion coefficient ($\Delta\alpha$) between inclusion and steel matrix. This can also be applied for the deformation behavior of different inclusions during hot rolling.

Since the decarburization occurs during the hot rolling and the related chemical composition of the steels changes, the dilation curves of both as-cast and hot-rolled samples are measured, the results are illustrated in Figure 10(a) and (b). The detected A_1 , A_3 , and M_s temperatures are summarized in Table III. As can be seen that A_1 and A_3 temperature slightly decrease with the increase of Mn content. Moreover, the cooling rate slightly influences M_s for all the samples. However, the value of M_s decreases with the increase of the Mn content in the steel. The A_3 for all the samples is lower than 800 °C (the ending temperature of hot rolling) and the M_s is less than 250 °C. These results indicate that the microstructure during the hot rolling temperature range is austenite but at room temperature is the martensite. In this case, α of austenite needs to be compared with that of inclusions.

The measured dilation curves with super low heating and cooling rates of 5 °C/min are used to calculate the coefficient of thermal expansion. The selection of these super low heating and cooling conditions is due to the α value needs to be measured with a condition closing to the equilibrium state. The results of α of different

samples are shown in Figure 11, which is calculated by Eq. [2].^[59] It is found that α of all the steels is with a similar level of about 25×10^{-6} .

$$\alpha_l(T) = \frac{1}{L_0} \frac{\partial L(T)}{\partial T}, \quad [2]$$

where α_l is the coefficient of thermal expansion in length, L_0 is the initial length of the material at room temperature, $\partial L(T)$ is the linear length changes at each temperature interval ∂T .

In order to compare the thermal expansion property between inclusion and the matrix, the values of α of different inclusions are presented in Figure 12, the data are from References 55 and 57. Therefore, the calculated values of $\Delta\alpha$ between MnS, MnSiO_3 and MnAl_2O_4 inclusions and the steel matrix are 6.9×10^{-6} , 15.4×10^{-6} and 17.1×10^{-6} , respectively. In the case of oxide inclusions, MnAl_2O_4 holds a much larger $\Delta\alpha$ in comparison to MnSiO_3 . In this case, MnAl_2O_4 hardly deforms during matrix deformation after the rolling process. It can be assumed that only elastic deformation occurs for MnAl_2O_4 inclusions based on their unchanged morphology during the rolling process. For the case of MnSiO_3 , it is homogeneous glassy silicate and is undergo plastic deformation during hot rolling. Due to the different deformability of MnAl_2O_4 and MnSiO_3 inclusions, these two phases gradually become separate from each other during hot rolling, see Figure 2. However, MnAl_2O_4 is in general found inside the MnSiO_3 inclusions, the aspect ratio of the whole oxide inclusion was defined by soft MnSiO_3 inclusion. For MnS inclusions, they have a much larger value of α which is closer to that of austenite and results in smaller $\Delta\alpha$ compared to oxide inclusions. Therefore, they are more easily deformed during hot rolling. To sum up, a smaller $\Delta\alpha$ between inclusions and austenite can lead to a larger deformation factors, *i.e.*, AR and DI during the hot rolling.

3. Correlation between physical properties of inclusions and mechanical property of steel

The morphology of inclusions after rolling has a large influence on the mechanical property of the steel product. The steel failure is described in terms of the nucleation, growth and coalescence of voids that are formed around inclusions.^[44] In this case, the fracture is more likely to be developed due to void coalescence with more fractured oxide inclusions. The deformation behaviors of different types of inclusions are schematically illustrated in Figure 13. The Mn(S,Se) inclusions are assumed to locate in the ductile region, where they experienced plastic deformation but without serious fracture. The MnAl_2O_4 inclusions are hardly deformed, it can be attributed to their high values of Young's modulus, micro-hardness and $\Delta\alpha$. The brittle to ductile transition temperature of MnSiO_3 inclusions is higher than the hot rolling temperature, so they are assumed to have small fracture toughness as they locate in the brittle region.^[24] Hence, they first undergo elastic deformation until the stress exceeded the elastic limit then they might also be crushed into smaller pieces during the rolling

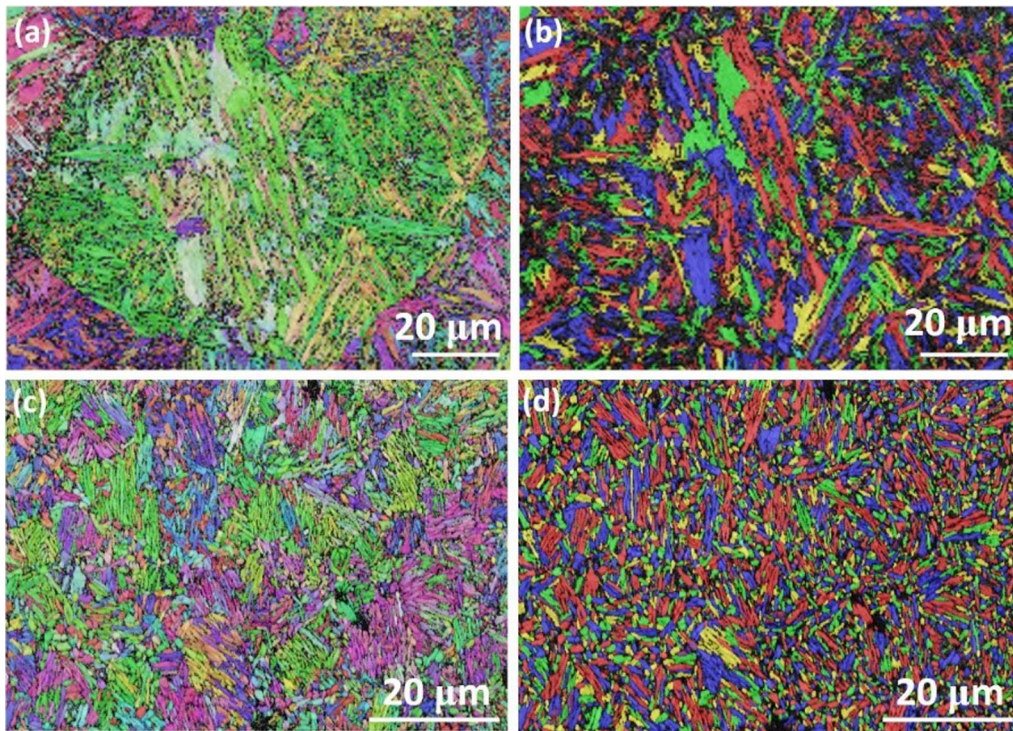


Fig. 14—EBSD analysis of MMS steel before and after hot-rolling, (a) inverse pole figure (IPF) and (b) random grain distribution (RGD) of MMS before rolling, and (c) inverse pole figure (IPF) and (d) random grain distribution of MMS after rolling. In IPF images, red, green and blue color represents [001], [101], and [111]. In RGD images, different color represents different grains, 5° of misorientation in grain maps is to define a grain boundary (Color figure online).

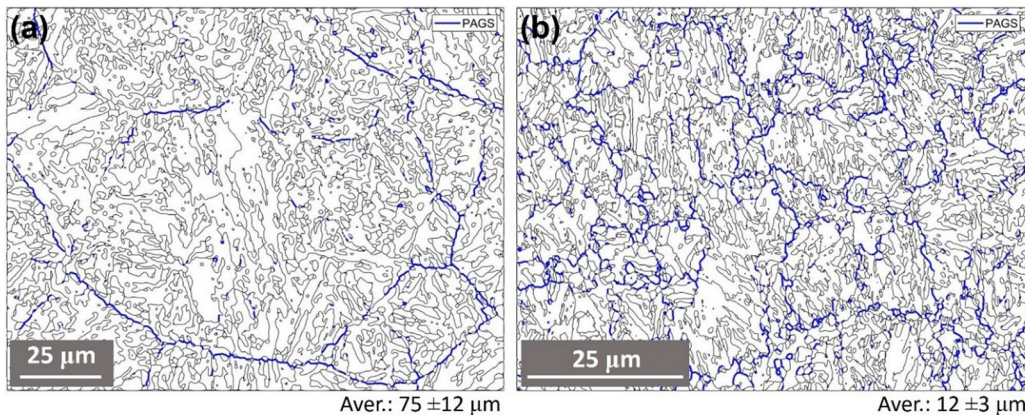


Fig. 15—Re-constructed prior austenite grain boundary (blue line) in the (a) as-cast and (b) hot-rolled steels (Color figure online).

Table IV. Summary of Obtained Empirical Expressions Between Inclusion Aspect Ratios and Other Parameters After Hot Rolling

	Relation between inclusion aspect ratio (AR) and plate thickness (PT)	Relation between inclusion aspect ratio (AR) and prior austenite grain size (PAGS)
MnS	$AR_{MnS} = (0.37 \pm 0.16) \times (P_C/P_R)$ (1)	$AR_{Mn(S,SE)} = (0.59 \pm 0.26) \times (P_C/P_R)$ (3)
MnSiO ₃	$AR_{MnSiO_3} = (0.23 \pm 0.12) \times (D_C/D_R)$ (2)	$AR_{MnSiO_3} = (0.37 \pm 0.19) \times (D_C/D_R)$ (4)

*AR_{MnS} and AR_{MnSiO₃} represent the aspect ratio of MnS and MnSiO₃ inclusions.
 **P_C and P_R represent the plate thickness of as-cast and hot-rolled steels.
 ***D_C and D_R represent prior austenite grain size of as-cast and hot-rolled steels.

process. Due to the difference in the deformability of MnAl_2O_4 and MnSiO_3 inclusions, micro-void can form between the oxide inclusion, followed by propagation of cracks, as shown in oxide and mixed types of inclusions. In the mixed inclusions, the deformations of $\text{Mn}(\text{S},\text{Se})$ inclusions are smaller than those single $\text{Mn}(\text{S},\text{Se})$ inclusions.

D. Correlation of Grain Size Evolution and Deformation of Inclusions After Hot Rolling

The correlation between the evolution of microstructure, *i.e.*, grain size and inclusion is presented in the last section. In order to quantitatively evaluate the correlation among the aspect ratio (AR) of different types of deformed inclusions (*i.e.*, liquid oxide (MnSiO_3) and sulfide ($\text{Mn}(\text{S},\text{Se})$) and the grain refinement after hot rolling, 7Mn steel is selected. This is due to the maximum and the average size of different types of deformed inclusions are almost same, thus the effect of heterogeneous inclusion size can be minimized. Figure 14 shows the EBSD images of the inverse pole figure (IPF) as well as the random grain distribution (RGD) analysis of as-cast and hot-rolled samples. The dominant structure of the steel is martensite, with a very small amount of retained-austenite (less than 5 pct). Briefly, it is seen that the prior austenite grain size (PAGS) as well as the thickness of martensite lath gets much smaller after hot-rolling. To quantitatively compare the microstructure feature, EBSD images of as-cast and hot-rolled steels are presented in the same magnification. However, the grain number is quite low in the as-cast one. To supply comprehensive information, a small magnification image with more grains is provided in supplementary Fig. S-1, which refers to electronic supplementary material.

In order to further analyze the correlation between the size of PAGS evolution and inclusion deformation, the prior austenite grain boundary is re-constructed based the EBSD data using MATLAB-based Toolbox METX, the result is shown as blue lines in Figure 15. It is seen that the average size of PAGS is around $75\ \mu\text{m}$ in the as-cast one, and around $12\ \mu\text{m}$ in the steel after hot-rolling. The obtained information in combination with AR ratio evolution in each kind of soft inclusion, *i.e.*, liquid oxide and sulfide, can be used to provide a quantitative correlation between inclusion, microstructure and the product parameter (*i.e.*, thickness of the plate) after hot-rolling. The results are shown in Table IV. It is a linear correlation and is obtained by the fitting method of each kind of deformed inclusion. The aim of providing these correlations is to evaluate the inclusion deformation ratio rapidly by checking the grain size evolution, since the grain size is much easier to measure compared to the aspect ratio of the specific kind of inclusion. The obtained understanding and empirical expressions aim to support the estimation and control different inclusion size evolution during the hot rolling.

V. CONCLUSIONS

The deformation behavior of different types of inclusions (*i.e.*, liquid oxide (MnSiO_3), MnAl_2O_4 , $\text{Mn}(\text{S},\text{Se})$, and complex oxy-sulfide) in medium Mn steels was investigated experimentally and theoretically. The deformation mechanisms of different types of inclusions were quantitatively discussed. The following conclusions were obtained:

1. The inclusions found in MMSs were classified into three categories: (1) $\text{Mn}(\text{S},\text{Se})$; (2) Oxide inclusions which consisting a core of MnAl_2O_4 and surrounded by liquid oxide (MnSiO_3); (3) Mixed inclusions containing oxide and $\text{Mn}(\text{S},\text{Se})$. Both liquid oxides and sulfide are able to be deformed during hot rolling.
2. The deformation behavior of different types of inclusions depends on their sizes as well as physical properties. When the maximum size of one type soft inclusion (*e.g.*, MnSiO_3) is much larger than another one (*e.g.*, $\text{Mn}(\text{S},\text{Se})$), oxide shows the larger deformation than that of $\text{Mn}(\text{S},\text{Se})$ where their size plays a dominant role than their physical properties. When the maximum size of different inclusions is similar, sulfide deforms more than MnSiO_3 does due to the joint influence of different physical properties. Specifically, inclusions with smaller values of micro-hardness and Young's modulus, and smaller difference in coefficient of thermal expansion between inclusions and matrix are more easily to be deformed.
3. Empirical correlations between the aspect ratio of different types of inclusion, grain size as well the thickness of plate after hot-rolling are provided based on the obtained experimental results. This information will contribute to understand and control of inclusion evolution in the medium Mn steels during the hot rolling process.

ACKNOWLEDGMENTS

W. Mu would like to acknowledge the Swedish Foundation for International Cooperation in Research and Higher Education (STINT, Projects No. PT2017-7330 & IB2020-8781) and Swedish iron and steel research office (Jernkontoret), in particular Gerhard von Hofstens Stiftelse för Metallurgisk Forskning for the financial support. National Natural Science Fund for Excellent Young Scientists (Project name: Intelligent Inclusion Metallurgy) is also acknowledged. Y. Wang and Y.G. Yang would like to acknowledge China Scholarship Council (CSC) and Jernkontoret. S. Lin (KTH, MSE) is acknowledged for assisting the EBSD analysis.

CONFLICT OF INTEREST

On behalf of all authors, the corresponding author states that there is no conflict of interest.

FUNDING

Open access funding provided by Royal Institute of Technology.

OPEN ACCESS

This article is licensed under a Creative Commons Attribution 4.0 International License, which permits use, sharing, adaptation, distribution and reproduction in any medium or format, as long as you give appropriate credit to the original author(s) and the source, provide a link to the Creative Commons licence, and indicate if changes were made. The images or other third party material in this article are included in the article's Creative Commons licence, unless indicated otherwise in a credit line to the material. If material is not included in the article's Creative Commons licence and your intended use is not permitted by statutory regulation or exceeds the permitted use, you will need to obtain permission directly from the copyright holder. To view a copy of this licence, visit <http://creativecommons.org/licenses/by/4.0/>.

SUPPLEMENTARY INFORMATION

The online version contains supplementary material available at <https://doi.org/10.1007/s11663-022-02517-2>.

REFERENCES

1. L. Holappa and O. Wijk: *Treatise on process metallurgy.*, 2014, pp. 347–72.
2. W. Wang, Y. Wang, W. Mu, J.H. Park, H. Kong, S. Sukenaga, H. Shibata, H. Larsson, and H. Mao: *Mater. Des.*, 2021, vol. 210, pp. 110097.
3. B. Hu, H. Luo, F. Yang, and H. Dong: *J. Mater. Sci. Technol.*, 2017, vol. 33, pp. 1457–64.
4. S.L. Chen, Z.X. Cao, C. Wang, C.X. Huang, D. Ponge, and W.Q. Cao: *J. Iron Steel Res. Int.*, 2019, vol. 26, pp. 1209–18.
5. W. Bleck: *Int. J. Miner. Metall. Mater.*, 2021, vol. 28, pp. 782–96.
6. J.H. Chu and Y.P. Bao: *Int. J. Miner. Metall. Mater.*, 2021, vol. 28, pp. 1288–97.
7. P. Gibbs, E. De Moor, M. Merwin, B. Clausen, J. Speer, and D. Matlock: *Metall. Mater. Trans. A.*, 2011, vol. 42A, pp. 3691–3702.
8. D.H. Kim, J.H. Kang, J.H. Ryu, and S.J. Kim: *Mater. Sci. Eng. A.*, 2020, vol. 774, pp. 138930.
9. P. Xie, M. Han, C. Wu, Y. Yin, K. Zhu, R. Shen, and J. Chen: *Mater. Des.*, 2017, vol. 127, pp. 1–7.
10. S.J. Park, B. Hwang, K. Lee, T.H. Lee, D.W. Suh, and H. Han: *Scripta Mater.*, 2013, vol. 68, pp. 365–69.
11. K. Kwon, I.C. Yi, Y. Ha, K.K. Um, J.K. Choi, K. Hono, K. Oh-Ishi, and N.J. Kim: *Scripta Mater.*, 2013, vol. 69, pp. 420–23.
12. G. Mishra, A. Chandan, and S. Kundu: *Metall. Mater. Trans. A.*, 2017, vol. 701A, pp. 319–27.
13. A. Grajcar, D. Woźniak, and A. Kozłowska: *Arch. Metall. Mater.*, 2016, vol. 61, pp. 811–20.
14. Z. Yu and C. Liu: *Metall. Mater. Trans. B.*, 2019, vol. 50B, pp. 772–81.
15. J.H. Park, D.J. Kim, and D.J. Min: *Metall. Mater. Trans. A.*, 2012, vol. 43A, pp. 2316–24.
16. H.X. Yu, D.X. Yang, J.M. Zhang, G.Y. Qiu and N. Zhang: *Int. J. Miner. Metall. Mater.*, 2022, vol. 29, pp. 256–62.
17. D.J. Kim and J.H. Park: *Metall. Mater. Trans. B.*, 2012, vol. 43B, pp. 875–86.
18. Y.B. Kang, M.S. Kim, S.W. Lee, J.W. Cho, M.S. Park, and H.G. Lee: *Metall. Mater. Trans. B.*, 2013, vol. 44B, pp. 309–16.
19. Y.G. Yang, W. Mu, X.Q. Li, H.T. Jiang, M. Wang, Z.L. Mi, and X.P. Mao: *J. Iron Steel Res. Int.*, 2022, vol. 29, pp. 316–26.
20. M. Xu, Y.G. Yang, J.Y. Chen, D. Tang, H.T. Jiang, and Z.L. Mi: *J. Iron Steel Res. Int.*, 2017, vol. 24, pp. 1125–30.
21. L. Zhang, C. Guo, W. Yang, Y. Ren, and H. Ling: *Metall. Mater. Trans. B.*, 2018, vol. 49B, pp. 803–11.
22. W. Yang, C. Guo, L. Zhang, H. Ling, and C. Li: *Metall. Mater. Trans. B.*, 2017, vol. 48B, pp. 2717–30.
23. G. Bernard, P. Ribound, and G. Urbain: *La Revue de Metalurgie-CTT.*, 1981, vol. 78, pp. 421–33.
24. W. Yang, K. Peng, L. Zhang, and Q. Ren: *J. Mater. Res. Technol.*, 2020, vol. 9, pp. 15016–22.
25. F.Y. Huang, Y.H.F. Su, and J.C. Kuo: *Met. Mater. Int.*, 2018, vol. 24, pp. 1333–45.
26. L. Dong and X. Liu: *Large Non-metallic Inclusions in Steel*, Metallurgical Industry Press, Beijing, 1991.
27. C. Luo and U. Ståhlberg: *Scand. J. Metall.*, 2002, vol. 31, pp. 184–90.
28. K. Wang, M. Jiang, X. Wang, W. Wan, and Y. Wang: *Metall. Mater. Trans. B.*, 2020, vol. 51B, pp. 95–101.
29. K. Wang, M. Jiang, X. Wang, Y. Wang, H. Zhao, and Z. Cao: *Metall. Mater. Trans. B.*, 2015, vol. 46B, pp. 2198–2207.
30. Y. Wang, L. Zhang, Y. Ren, Z. Li, C. Slater, K. Peng, F. Liu, and Y. Zhao: *Steel Res. Int.*, 2021, vol. 92, p. 2000609.
31. Y. Wang, L. Zhang, Y. Ren, Z. Li, C. Slater, K. Peng, F. Liu, and Y. Zhao: *J. Mater. Res. Technol.*, 2021, vol. 11, pp. 1220–31.
32. J.S. Park and J.H. Park: *Steel Res. Int.*, 2014, vol. 85, pp. 1303–09.
33. F. Bachmann, R. Hielscher and H. Schaeben: Texture analysis with MTEX—free and open source software toolbox. In Proceedings of Solid State Phenomena, 2010, pp. 63–68.
34. F. Bachmann, R. Hielscher, and H. Schaeben: *Ultramicroscopy.*, 2011, vol. 111, pp. 1720–33.
35. S. Huang, Z. Dong, W. Mu, V. Ström, G. Chai, and L. Vitos: *Appl. Phys. Lett.*, 2020, vol. 117, p. 164101.
36. J.-O. Andersson, T. Helander, L. Höglund, P. Shi, and B. Sundman: *Calphad.*, 2002, vol. 26, pp. 273–312.
37. TCS Steels/Fe-Alloys Database Version 10.1, (TCFE10), Stockholm, June 2020.
38. P. Hohenberg and W. Kohn: Density functional theory (DFT). *Phys. Rev.*, 1964, vol. 136, pp. B864.
39. L. Vitos: *Phys. Rev. B.*, 2001, vol. 64, pp. 014107.
40. L. Vitos: Springer Science & Business Media, 2007.
41. Z. Dong, S. Schönecker, D. Chen, W. Li, S. Lu, and L. Vitos: *Int. J. Plast.*, 2019, vol. 119, pp. 123–39.
42. X. Fan, S. Xi, D. Sun, Z. Liu, J. Du, and C. Tao: *Hydrometallurgy.*, 2012, vol. 127, pp. 24–29.
43. R. Kiessling and N. Lange: *The Metals Society of London*. UK, 1968, pp. 17–25.
44. N. Choi, K. Lim, Y. Na, U. Glatzel, and J. Park: *J. Alloys Compd.*, 2018, vol. 763, pp. 546–57.
45. W. Mu, N. Dogan, and K.S. Coley: *Metall. Mater. Trans. B.*, 2017, vol. 48B, pp. 2379–88.
46. W. Mu, N. Dogan, and K.S. Coley: *Metall. Mater. Trans. B.*, 2017, vol. 48B, pp. 2092–2103.
47. T. Malkiewicz and S. Rudnik: *J. Iron Steel Inst. Jpn.*, 1963, vol. 201, pp. 33–38.
48. K.I. Yamamoto, H. Yamamura, and Y. Suwa: *ISIJ Int.*, 2011, vol. 51, pp. 1987–94.
49. P. Ahmadian and M. Taghizadeh: *Metall. Mater. Eng.*, 2020, vol. 26, pp. 43–55.
50. H.L. Yu, C. Lu, K. Tieu, and G.Y. Deng: *J. Comput. Theoret. Nanosci.*, 2012, vol. 9, pp. 1745–49.
51. J. Tse: *J. Superhard Mater.*, 2010, vol. 32, pp. 177–91.
52. D. Brooksbank and K. Andrews: Production and application of clean steels. *Lond. Iron Steel Inst.*, 1972, vol. 287, pp. 186–98.
53. S. Kishimoto, A. Koyama and H. Tanaka: Glass-ceramics, process for producing the same, and substrate for information recording medium, information recording medium and information recording device each using the glass-ceramics. Google Patents, 2002.
54. E. Bruschini, S. Speziale, G.B. Andreozzi, F. Bosi, and U. Hålenius: *Am. Miner.*, 2015, vol. 100, pp. 644–51.

55. X. Chen, J. Ou, Y. Kang, Z. Huang, H. Zhu, G. Yin, and H. Wen: *J. Mater. Sci.: Mater. Med.*, 2008, vol. 19, pp. 1257–63.
56. D. Ladutkin, E. Korte, M. Bleymehl, C. Bruch, and K.G. Doppler: *In Bearing Steel Technologies: 11th Volume, Advances in Steel Technologies for Rolling Bearings*, ASTM International, New York, 2017.
57. N. Ånmark, A. Karasev, and P.G. Jönsson: *Materials.*, 2015, vol. 8, pp. 751–83.
58. X. Jiang, J. Zhao, and X. Jiang: *Comput. Mater. Sci.*, 2011, vol. 50, pp. 2287–90.
59. W.D. Callister and D.G. Rethwisch: *Fundamentals of Materials Science and Engineering: An Integrated Approach*, 3rd ed. Wiley, New York, 2008, pp. 708–10.

Publisher's Note Springer Nature remains neutral with regard to jurisdictional claims in published maps and institutional affiliations.